International Journal of Applied Earth Observation and Geoinformation 119 (2023) 103313

Contents lists available at ScienceDirect

International Journal of Applied Earth Observation and Geoinformation

journal homepage: www.elsevier.com/locate/jag

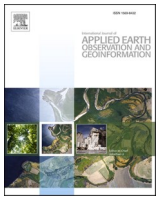

Potentiality of SDGSAT-1 glimmer imagery to investigate the spatial variability in nighttime lights

Biyun Guo [a,b], Deyong Hu [a,b,*], Qiming Zheng [c,d]

[a] College of Resource Environment and Tourism, Capital Normal University, Beijing 100048, China
[b] Beijing Key Laboratory of Resource Environment and Geographic Information System, Beijing 100048, China
[c] Department of Land Surveying and Geo-Informatics, The Hong Kong Polytechnic University, Hung Hom, Kowloon, Hong Kong
[d] Center for Nature-based Climate Solutions, National University of Singapore, 14 Science Drive 4, Singapore 117543, Singapore

ARTICLE INFO

Keywords:
Nighttime lights
SDGSAT-1
ISS-P
Multispectral
Land use type
Urbanization

ABSTRACT

The successful launch of Sustainable Development Science Satellite 1 (SDGSAT-1) complements the existing nighttime lights (NTL) data with high spatial resolution in the three visible bands (40 m) and the panchromatic band (10 m). This study aimed to evaluate the potentiality of the new NTL imagery – SDGSAT-1 – in revealing the spatial variation in NTL intensity. We compared the NTL image from SDGSAT-1 with other existing NTL datasets: the Visible infrared Imaging Radiometer Suite-Day Night Band (VIIRS-DNB), Luojia1-1 (LJ1-01), and photographs from the International Space Station (ISS-P) at spatial resolutions of 500 m, 130 m, and 10 m, respectively. Then, we investigated the intraurban NTL spatial variability of eleven urban land-use types with analysis of variance (ANOVA). In addition, we used random forest (RF) regression to analyze the relationship between explanatory factors and NTL variation. The results showed the following: (1) The quality of the SDGSAT-1 NTL image was comparable with ISS-P and better than VIIRS-DNB and LJ1-01 imagery in spectral and spatial resolution. (2) The ability of the RGB bands and grayscale brightness of the SDGSAT-1 NTL image to distinguish various land use types outperformed that of the ISS-P, LJ1-01, and VIIRS-DNB images. (3) The NTL spectral index SONDI, combined with three visible bands, could improve the ability of a single band to show the lighting differences in intraurban areas. (4) The nine variables explained 39.20%–42.30% of the NTL intensity variability in the four RF models. Road density and public POI density were the most important variables in the red-green and blue bands, indicating that high-pressure sodium and lighting-emitting diode lamps were primarily deployed in the road and public areas, respectively. Meanwhile, the potential applications of SDGSAT-1 NTL imagery were further discussed. Our findings indicate the great potential of SDGSAT-1 NTL imagery for supporting sustainable urban development.

1. Introduction

Night-time lights (NTL) could be regarded as the novel footprints of urbanization in extent and intensity. Numerous studies have shown that NTL data can be applied in multiple aspects, including mapping urban areas (Li et al., 2018b; Zhou et al., 2018), estimating urban socioeconomic parameters (Chen et al., 2022; Zhao et al., 2020), and monitoring armed conflicts (Li et al., 2017). Moreover, there are large-scale lighting facilities that transition from low-pressure sodium (LPS) and high-pressure sodium (HPS) to light-emitting diodes (LED) in urban areas. This produces more blue lighting (Elvidge et al., 2007). Some research has noted that overdue lighting adversely impacts human health and the ecosystem, especially blue lighting (Gaston and de Miguel, 2022; Sánchez de Miguel et al., 2022). Given the global light transformation and its significant influence (Levin et al., 2020), it is imperative to develop a more effective technique for accurately observing NTL in spatial and spectral information.

Currently, there are diverse approaches to capturing the intensity and extent of NTL. The first free NTL remote sensing data were from the Defense Meteorological Satellite Program-Operational Linescan System (DMSP-OLS) sensor in 1992 (Elvidge et al., 1997). Subsequently, two datasets with higher spatial resolutions, wider dynamic ranges, and fewer issues (saturation and blooming) were acquired from the Visible Infrared Imaging Radiometer Suite-Day Night Band (VIIRS-DNB) and

* Corresponding author.
E-mail addresses: biyunguo@cnu.edu.cn (B. Guo), deyonghu@cnu.edu.cn (D. Hu), qmzheng@zju.edu.cn (Q. Zheng).

https://doi.org/10.1016/j.jag.2023.103313
Received 19 February 2023; Received in revised form 4 April 2023; Accepted 15 April 2023
Available online 25 April 2023

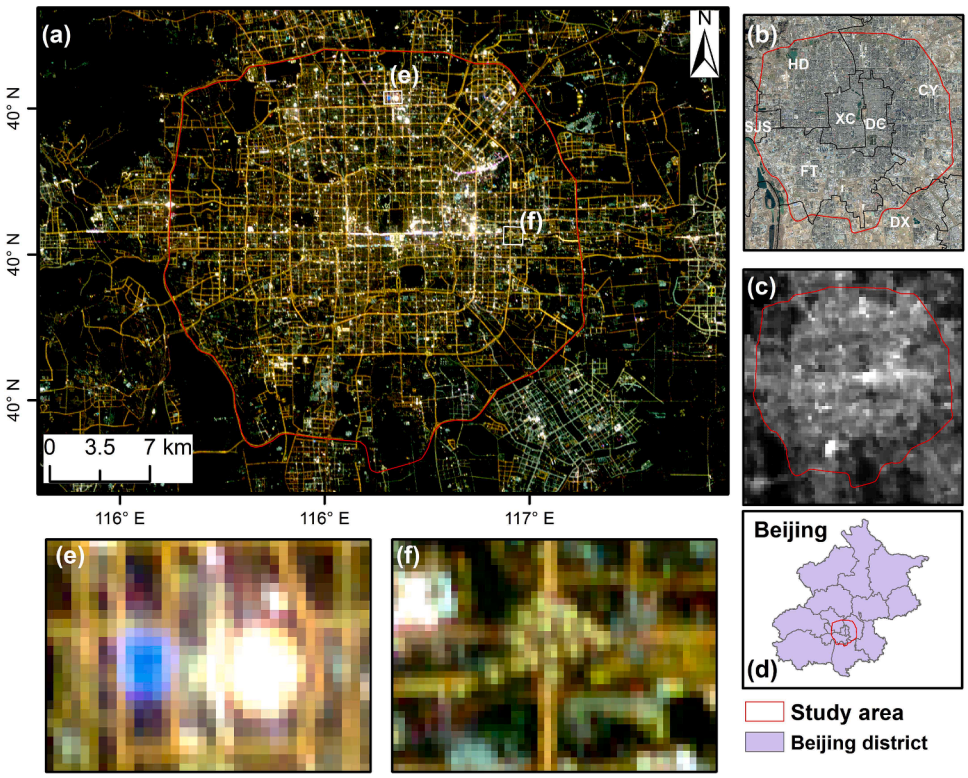

Fig. 1. SDGSAT-1 NTL image (a), Landsat 8 OLI image (b), VIIRS-DNB NTL image (c), the location of the study area (d), and subsets of selected areas (e-f) in the SDGSAT-1 NTL image. The three visible bands (red, green, and blue, RGB) are used to composite the SDGSAT-1 NTL image. (For interpretation of the references to color in this figure legend, the reader is referred to the web version of this article.)

Luojia1-01 (LJ1-01) in 2012 (Elvidge et al., 2013) and 2018 (Li et al., 2018b), respectively. These satellite NTLs with a single spectral band provide valuable information to describe the spatial–temporal characteristics of urban human footprints at large scales (Zhang et al., 2013; Zheng et al., 2021). However, three issues need to be taken into consideration: (1) the lack of multispectral bands, (2) the DMSP-OLS composite product including visible and near-infrared (NIR) ranges (400–1100 nm) but with 1 km spatial resolution, and (3) LJ1-01 (460–980 nm) and VIIRS-DNB (505–890 nm) imagery with higher spatial resolution but missing information from blue lighting. Therefore, we need new NTL data with multiple spectra and high spatial resolution to complement the existing NTL data and collect more comprehensive and finer artificial lighting radiance information.

Photography from the International Space Station (ISS-P) and JL1-3B can collect colorful lights in contrast to the three NTLs above (Elvidge et al., 2007). These two multispectral NTLs have been successfully applied in population estimation (Li et al., 2018a), lighting pollution monitoring (Sánchez de Miguel et al., 2019), lighting source classification (Zheng et al., 2018), and analyzing NTL spatial variability in land uses (Guk and Levin, 2020). Although these two multispectral NTL datasets have been applied in finer urban studies, they still face some drawbacks to overcome. ISS-P imagery (https://eol.jsc.nasa.gov/) lacks the stability of image time, geographic information, and radiation correction. JL1-3B NTL imagery (https://www.jl1mall.com/SatelliteImagery/NightLight) is geared more toward commercial than broad scientific needs. Therefore, using suitable multispectral NTL imagery at a low cost and stability is essential for urban applications.

A novel free satellite-derived NTL, Sustainable Development Science Satellite 1 (SDGSAT-1), has three visible bands and a panchromatic band with spatial resolutions of 40 m and 10 m, respectively (Guo et al., 2023). The SDGSAT-1 satellite was launched by the Chinese Academy of Sciences on November 5, 2021. SDGSAT-1 is in a sun-synchronous orbit with an orbit altitude of 505 km and a swath of 300 km. Recently, it was used to evaluate public perception of urban NTL and found to be negatively correlated with the proportion of blue lighting in Beijing (Lin et al., 2023). In addition, some studies have demonstrated that SDGSAT-1 NTL has the potential to quantify nighttime aerosols (Wang et al., 2023) and extract road information (Chang et al., 2022). According to the concept of Nightsat (Elvidge et al., 2007), NTL data with three to five spectral bands and fine spatial resolution (50–100 m) would enable more quantitative applications and the detection of lighting type conversions. Therefore, the potential of SDGSAT-1 NTL data is worthwhile to investigate on finer urban scales.

One important urban development policy, urban renewal, has resulted in profound changes in intraurban environments in China (Fu et al., 2019; Liu et al., 2020). Notably, the urban renewal process results in changes in land use types, as in Yongqingfang, Guangzhou, where residential areas are converted into commercial and public spaces owing to this urban policy (Wang et al., 2022). Therefore, urbanization, especially intraurban renewal, significantly shapes land-use functions, as well as the NTL pattern therein. However, existing studies have mainly examined the relationship between panchromatic NTL brightness and land use types (Jin et al., 2019; Ma, 2018). The intraurban variations in NTL properties across land use types have not been studied thoroughly.

Therefore, this study aimed to analyze the intraurban spatial variability in multispectral NTL intensity and spectra at parcel-level land use scales using SDGSAT-1 NTL imagery with high spatial resolution, taking the capital of China, Beijing, as the study area. First, we compared SDGSAT-1 NTL imagery with other existing NTL data in terms of their spatial pattern and pixel brightness to assess the data quality of SDGSAT-1. Second, we applied the analysis of variance (ANOVA) technique to test the potentiality of SDGSAT-1 NTL imagery to investigate the spatial variability in NTL across land-use types. Third, we used the random forest (RF) regression method to analyze the explanatory factors underlying the NTL variations.

Table 1
Comparison of three multispectral NTL datasets.

Type	ISS-P	JL1-3B	SDGSAT-1
Satellite launch time	—	2017–01–09	2021–11–5
Availability	2003–	2017–	2021–
Spectral resolution	—	Blue:430–512 nm Green:489–585 nm Red:580–720 nm	Panchromatic:450–900 nm Blue:430–520 nm Green:520–615 nm Red:615–900 nm
Spatial resolution	5–200 *m*	0.92 *m*	40 m (Visible bands) 10 m (Panchromatic band)
Free	Yes	No	Yes
Overpass (local time)	—	~22:00	~21:00
Temporal resolution	Irregular	4.5 days	11 days
Radiometric Resolution	8–14 bits	8 bits	16 bits

2. Study area and datasets

2.1. Study area

Our study area focused on the metropolitan region (the 5th Ring Road area), which included seven districts in Beijing, China: Xicheng (XC), Dongcheng (DC), Haidian (HD), Chaoyang (CY), Shijingshan (SJS), Fengtai (FT), and Daxing (DX) (Fig. 1). The metropolitan region covers an area of 667.21 km^2 and accommodates almost half of the residential population of Beijing. Meanwhile, there are diverse human activities at night, including commercial, political, educational, recreational, and cultural events (Fig. 1a). Since various lighting lamps were distributed in different human activity zones, there was multicolor lighting, dominated by yellow lights, with minor green, white, blue, and magenta areas.

2.2. Datasets and preprocessing

The SDGSAT-1 NTL imagery had high spatial resolution and multispectral bands. The significant advancements brought about by SDGSAT-1 compared with the two multispectral NTLs, ISS-P and LJ1-3B, are listed in Table 1 below: (1) wider spectral range, including 430–520 nm (blue), 520–615 nm (green), 615–900 nm (red), and 450–900 nm (panchromatic band); (2) higher radiometric resolution (16 bits); and (3) earlier overpass time (approximately 21:00). To date, owing to limited data availability, only one high-quality, cloud-free, and stripe-free scene was acquired for Beijing on 26 November 2021 via the International Research Center of Big Data for Sustainable Development Goals (https://data.casearth.cn/thematic/brics_2022_china/143). The SDGSAT-1 NTL images did not perform radiance correction, mainly because the parameters of the radiance correction are not yet unreliable. Additionally, the study does not involve explicit physical parameter estimation; therefore, it is reasonable to use digital number (DN) values for analyzing NTL variability (Guk and Levin, 2020).

Additionally, three cloud-free NTL scenes, ISS-P (ISS061-E-123062, 22:25:00 overpass time), LJ1-01, and version 1 monthly VIIRS-DNB, were acquired on 12 January 2020, 27 September 2018, and November 2020, respectively. These three NTL data were used to examine the quality of SDGSAT-1 NTL data. Importantly, the land use map covering 11 types at the parcel level (Fig. 2) was obtained from Gong et al. (2020). Moreover, a Landsat OLI 8 image on 12 December 2021 was used to generate the normalized difference vegetation index (NDVI). Points of interest (POIs) in 2022 were crawled from Amap (https://www.amap.com/). Road network and building vector data in 2021 were obtained from the Open Street Map. These three datasets were used to explain the spatial variability of SDGSAT-1 NTL in intensity and spectrum. Table 2 shows all the data used and their preprocessing.

All data were reprojected to the WGS_1984_UTM_zone_50N coordinated system. Then, two multispectral NTL datasets, SDGSAT-1 and ISS-P, need to compute the grayscale brightness (Eq. (1) to quantify the magnitude of NTL, which is effective at enhancing contrast and avoiding noise, contouring, and halo artifacts (Grundland and Dodgson, 2007).

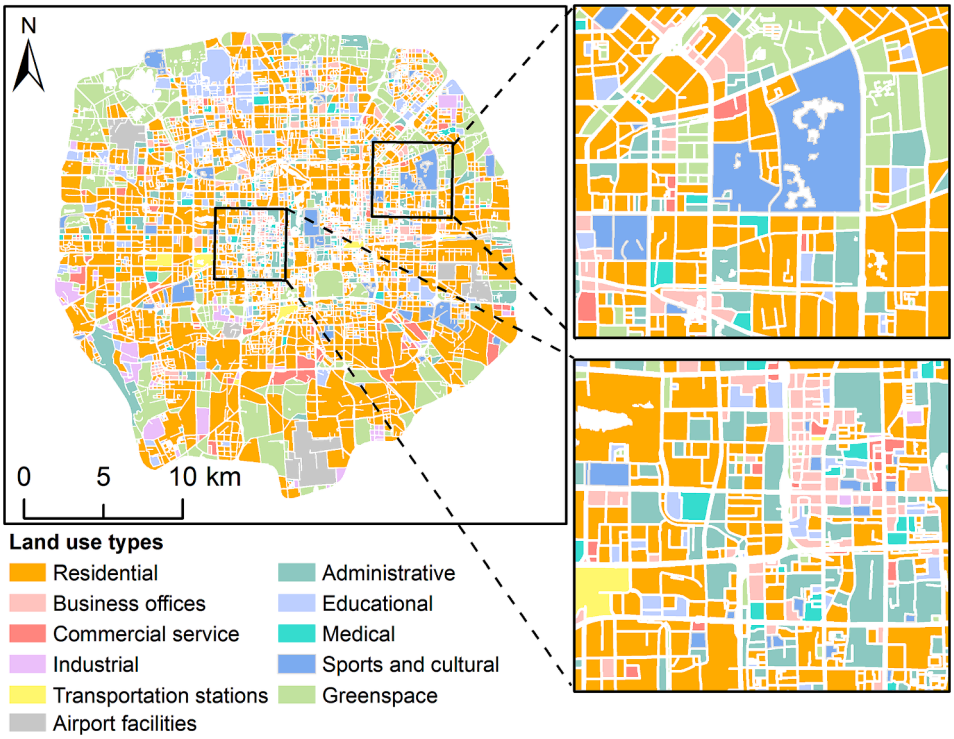

Fig. 2. Parcel-level land use map (Gong et al., 2020).

Table 2
Properties of the data and related preprocessing.

Type	Time	Spatial resolution	Preprocessing
SDGSAT-1 (RGB)	26/11/2021 (DD/MM/YYYY)	40 *m*	Grayscale brightness
ISS-P	12/01/2020 (DD/MM/YYYY)	10 *m*	Geometric correction and grayscale brightness
LJ1-01	27/09/2018 (DD/MM/YYYY)	130 *m*	Radiometric and geometric correction
VIIRS-DNB	11/2020 (MM/YYYY)	500 *m*	Noise elimination
Landsat 8 OLI	12/12/2021 (DD/MM/YYYY)	30 *m*	True color composite/NDVI composition
Land use map	2018 (YYYY)	–	–
POI	2022 (YYYY)	–	Reclassify/density analysis
Road network	2021 (YYYY)	–	
Building polygon	2021 (YYYY)	–	Rasterization

$$Brightness = 0.2989 \times Red + 0.5870 \times Green + 0.1140 \times Blue \quad (1)$$

where Brightness denotes the grayscale brightness of multispectral NTL images, and *Red*, *Green*, and *Blue* are the DN values of each corresponding band. The primary reason for not using the panchromatic band of SDGSAT-1 NTL data was to reduce information loss from blue light owing to the blue spectral range of the panchromatic band (450–900 nm) being shorter than that of the blue band (430–520 nm, Table 1).

The ISS-P and LJ1-01 images were subjected to a geometric correction (Jiang et al., 2018; Li et al., 2018a). Their correction accuracy was measured by the root mean standard error (RMSE) of 9.65 m and 19.48 m, respectively. Meanwhile, radiometric correction (Li et al., 2019) was used to obtain radiance intensity from the DN value on LJ1-01 NTL (Eq. (2)). Noise elimination was performed in the monthly VIIRS-DNB NTL to overcome the background and abnormally high noises using a background mask (version 2 annual lit mask in 2020) and local median filter, respectively (Elvidge et al., 2021)

$$L = DN^{\frac{3}{2}} \times 10^{-10} \times w \times 10^{5} \quad (2)$$

where w is the bandwidth, ranging from 460 to 980 nm, w was set to 0.52 μm, and L denotes the absolute radiance brightness value (nW/cm^2/sr).

POI data were reclassified into five classes, including residential land, commercial land, industrial land, public management and service land, and greenspace. Road network data were chosen into four classes, e.g., primary, secondary, tertiary, and trunk. Then, POI and road network data were performed for kernel density analysis to generate a smooth raster surface, which reflected the density of various POIs and roads. Building polygon data were rasterized into building height and density raster data. The above raster data were in 40 m correspondence with SDGSAT-1 NTL data.

3. Methods

In this study, we develop a framework for investigating the potential of SDGSAT-1 NTL to reveal the spatial variability of NTL intensity across 11 land use types using multisource geography and remote sensing data. The flowchart for this investigation is shown in Fig. 3. The entire process consisted of three steps: (1) Quality analyses of the SDGSAT-1 NTL with the other three NTLs using two criteria: spatial pattern and pixel-level correlation. (2) Using the ANOVA method, we computed mean NTL values and three NTL spectral indexes to explore the spatial variability of each visible band and the combination of two or three bands. (3) We modeled the relationship between the nine explanatory variables and the response variable using the RF algorithm to identify the suitable reasons for NTL variability.

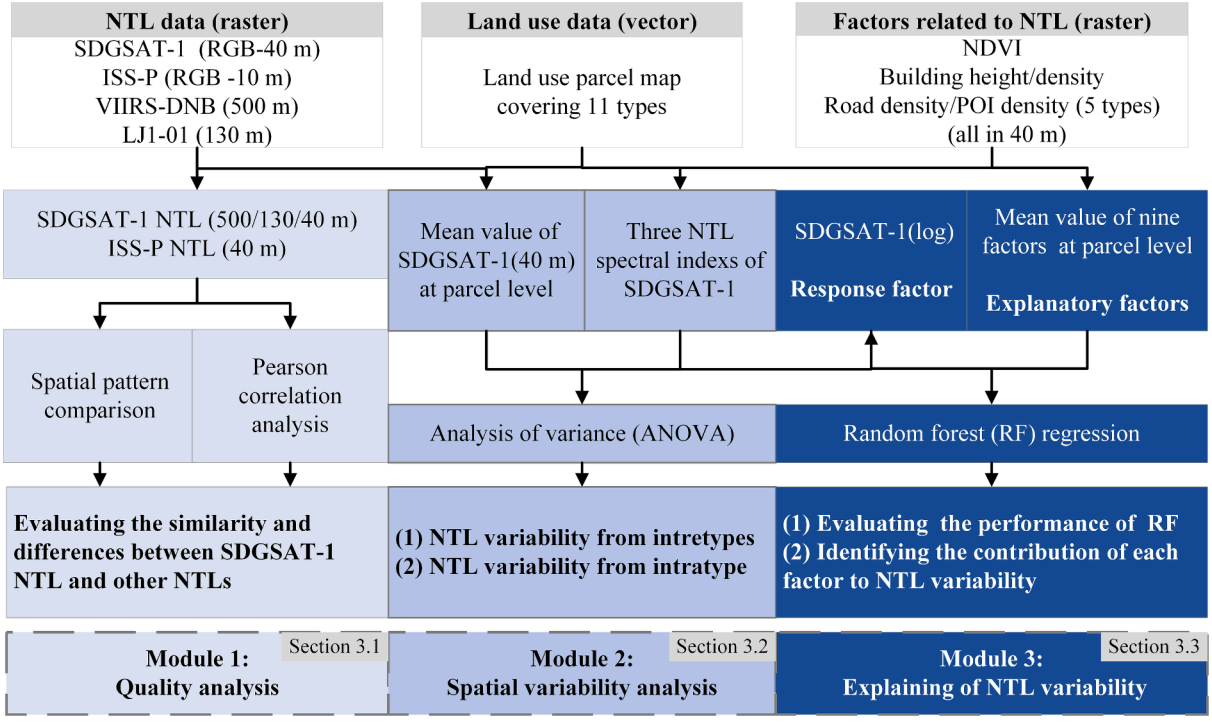

Fig. 3. Schematic view for evaluating the potential of SDGSAT-1 NTL in revealing the spatial variability of NTL intensity at the land use parcel level.

Table 3
The explanatory factors related to NTL intensity.

Type	Factor	Number
Physical nature	Normalized Difference Vegetation Index (NDVI)	1
Human activity	Residential POI Density (RPOID)	5
	Commercial POI Density (CPOID)	
	Industrial POI Density (IPOID)	
	Public POI Density (PPOID)	
	Greenspace POI Density (GPOID)	
Infrastructure	Building Density (BD)	3
	Building Height (BH)	
	Road Density (RD)	

3.1. Comparison analyses examining the quality of SDGSAT-1 NTL imagery

We conducted a series of comparisons, including spatial patterns and correlations between SDGSAT-1 and other NTL data, to examine the quality of the SDGSAT-1 glimmer imagery. First, we compared single-band NTL data, i.e., VIIRS-DNB and LJ1-01, with SDGSAT-1. The pixel sizes of SDGSAT-1 NTL data were resampled to 500 m and 130 m using the mean aggregation method. The SDGSAT-1 NTL brightness was then calculated using the mean values of the red and green bands (Guk and Levin, 2020). Since VIIRS-DNB and LJ1-01 do not include the blue spectrum, the blue band was not included during the procedure (Elvidge et al., 2013; Li et al., 2018b). The values from the three NTL data were extracted using fishnet points at 500 m and 130 m scales, and the Pearson correlation coefficient (r) was computed at two spatial scales. Second, the comparison of multispectral NTL data, i.e., SDGSAT-1 and ISS-P, was performed by resampling the cell size of ISS-P to 40 m. Then, they both have three visible bands and grayscale brightness at the same spatial resolution. The values from these two NTL datasets were also extracted by the fishnet points at 40 m. The r was then determined for each cell size between identical bands.

$$r = \frac{\sum_{i=1}^{n}(X_i - \overline{X})(Y_i - \overline{Y})}{\sqrt{\sum_{i=1}^{n}(X_i - \overline{X})^2}\sqrt{\sum_{i=1}^{n}(Y_i - \overline{Y})^2}} \tag{3}$$

where n is the number of all the pixels; X_i and Y_i denote SDGSAT-1 and the other NTL data values at the i-th pixel; and $\overline{X}$ and $\overline{Y}$ denote the average value of SDGSAT-1 and the other NTL data in all the pixels. The other NTL data denote VIIRS-DNB, LJ1-01, and ISS-P. The higher the r-value, the higher the similarity between SDGSAT-1 NTL and other NTL data.

3.2. Analysis of spatial variability in NTL

To examine the spatial variability in SDGSAT-1 NTL imagery at parcel-level land uses, ANOVA was conducted. First, the mean values for the three bands (RGB) and the grayscale brightness of SDGSAT-1 NTL at a spatial resolution of 40 m at the parcel level were calculated using the zonal statistical method. Then, ANOVA was conducted on the mean brightness in 11 land use types to examine the differences between various land use types. The differences in NTL were analyzed from intertypes and intratype, i.e., the ANOVA letters of mean NTL value of all the land-use types and the relative ranks of three visible bands in the same land-use type. Furthermore, ISS-P, LJ1-01, and VIIRS-DNB were subjected to ANOVA to illustrate their ability to distinguish land uses and further show the advantages of SDGSAT-1.

To improve the NTL variations between different land use types, three NTL spectral indexes were proposed, including the Normalized Difference Index between Greens and Reds (NDIGR, Eq. (4), the Normalized Difference Index between Blues and Greens (NDIBG, Eq. (5), and the sum of NDIGR and NDIBG (SONDI, Eq. (6).

$$NDIGR = (Green - Red)/(Green + Red) \tag{4}$$

$$NDIBG = (Blue - Green)/(Blue + Green) \tag{5}$$

$$SONDI = NDIGR + NDIBG \tag{6}$$

where Red, Green, and Blue denote the corresponding bands of the SDGSAT-1 NTL image.

3.3. Explaining factors of spatial variability in NTL

Nine factors spanning physical nature, human activity, and infrastructure (Table 3) were utilized to explain the mean values of RGB bands and brightness at the parcel level in 40 m SDGSAT-1 NTL data. Additionally, each response variable underwent a logarithmic modification to make the data closer to a normal distribution (Guk and Levin, 2020). The relationships between the explanatory factors and the response variable were established using the RF model. It has been demonstrated that the RF model outperforms traditional machine learning algorithms in geospatial and remote sensing applications like regression and classification (Belgiu and Drăgu, 2016; Yang et al., 2022). Four models in total were conducted to understand the causes of NTL variability in spectrum and intensity. In four RF models, 90% of the parcels were chosen randomly to be trained, and the remaining 10% were left to validate the model's performance. R^2 (Eq. (7) and RMSE (Eq (8) were used to assess how well the RF models worked. In the process of training RF models, importance scores were used to illustrate the association between the response variable and explanatory variables (Hu et al., 2022), to quantify the contribution of each variable to NTL variability and to identify the main contributors:

$$R^2 = 1 - \frac{\sum_{i=1}^{m}(\hat{y}_i - y_i)^2}{\sum_{i=1}^{m}(y_i - \overline{y})^2} \tag{7}$$

$$RMSE = \sqrt{\frac{1}{m}\sum_{i=1}^{m}(y_i - \hat{y}_i)^2} \tag{8}$$

where m is the total number of land use parcels, y_i and $\hat{y}_i$ denote the brightness values of the i-th parcel in the SDGSAT-1 NTL and predicted NTL from the RF models, and $\overline{y}$ denotes the mean value of SDGSAT-1 DN for m parcels.

4. Results

4.1. Comparability analysis of SDGSAT-1 NTL imagery

4.1.1. Comparison of single-band NTL and SDGSAT-1 NTL imagery

The spatial pattern and correlations were compared between the two single-band NTLs and the SDGSAT-1 NTL image. Visually, SDGSAT-1 maintained a similar trend with VIIRS-DNB and LJ1-01. From the urban center region to the outskirts, the NTL intensity decreased at a scale of 500 m (Fig. 4a-b). The urban structure could be depicted more clearly in LJ1-01 and SDGSAT-1 at a 130 m scale (Fig. 4c-d) than in Fig. 4(a-b). Furthermore, with the fine spatial resolution, more dark pixels could be observed in urban areas. This illustrates the spatial scale effect of remote sensing observation data to some degree. Because the differences between the two NTL data were enlarged with the finer resolution, the correlation of SDGSAT-1 and VIIRS-NDB (r = 0.57, Fig. 4e) was higher than that of SDGSAT-1 and LJ1-01 (r = 0.51, Fig. 4f). In addition, the structure of urban elements, such as road networks, was more apparent in the SDGSAT-1 images than in the other two NTLs with the same resolution (Fig. 4a-d). Therefore, the quality of SDGSAT-1 NTL

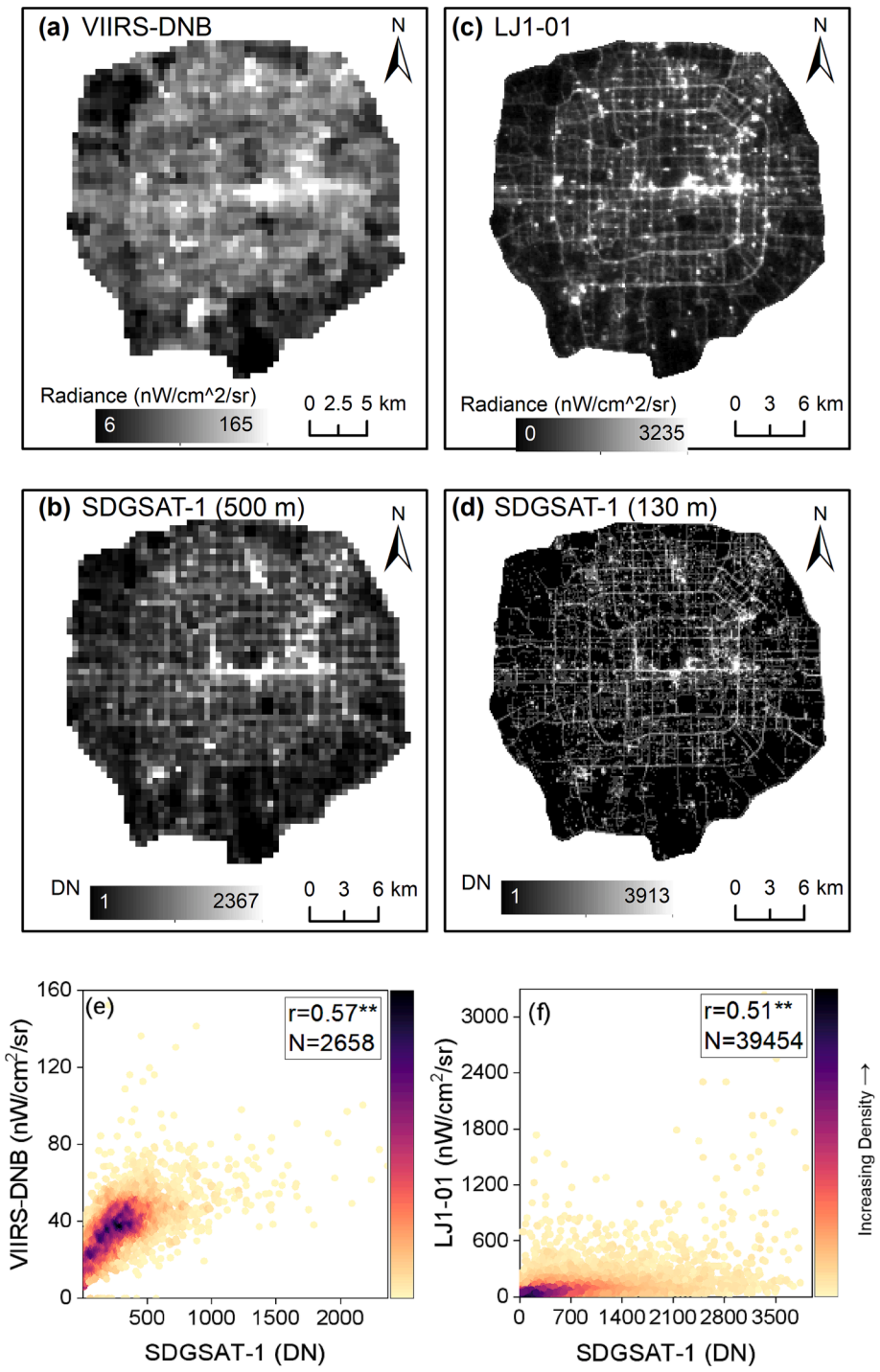

Fig. 4. Comparison of VIIRS-DNB, LJ1-01, and SDGSAT-1 NTL. Spatial pattern (a-d) of VIIRS-DNB, SDGSAT-1 at 500 m, LJ1-01, and SDGSAT-1 at 130 m. Scatter plot between SDGSAT-1 at 500 m and VIIRS-DNB (e) and between SDGSAT-1 at 130 m and LJ1-01 (f). The symbol ** indicates that the correlation is significant at the 0.01 level (two-tailed).

imagery was higher than that of VIIRS-DNB and LJ1-01 in discerning urban morphology.

4.1.2. Comparison of ISS-P and SDGSAT-1 NTL imagery

The comparisons of two multispectral NTLs, ISS-P and SDGSAT-1, at 40 m are shown in Fig. 5. In terms of the spatial distribution of red, green, and blue channels, SDGSAT-1 NTL displayed good correspondence with ISS-P. Moreover, their differences were represented in three bands' lit area and intensity values (Fig. 5a-f). Owing to the atmospheric scattering of the blue band, the brightness of the blue band (Fig. 5e-f) was weaker than that of the red (Fig. 5a-b) and green (Fig. 5c-d) bands. The spatial distribution area of the blue band in bright was also less than that of the other two bands. This may correlate with the distribution of LED lamps because they are the primary source of blue light (Guk and Levin, 2020; Zheng et al., 2018). In the multispectral NTL, the colors of the SDGSAT-1 image (Fig. 5g) and ISS-P (Fig. 5h) exhibited obvious differences owing to the variability of imaging with different sensors. The correlation degree of SDGSAT-1 and ISS-P in different bands ranged from 0.46 to 0.60 (Fig. 5i-m). The linear correlations in the blue band and red band were weakest (r = 0.46, Fig. 5k) and strongest (r = 0.60,

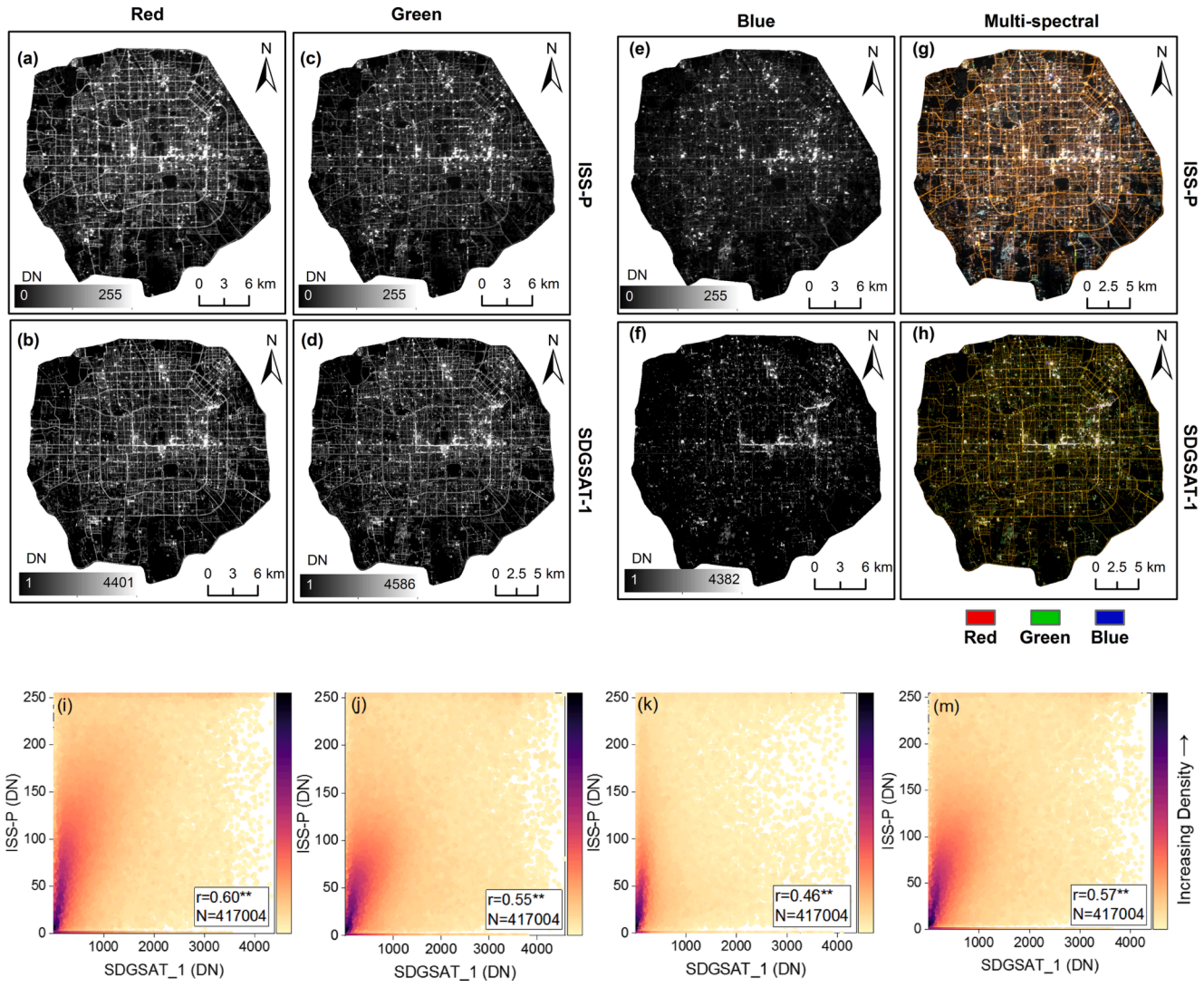

Fig. 5. Spatial comparison of SDGSAT-1 and ISS-P in the red (a-b), green (c-d), and blue bands (e-f) and multispectral NTL imagery (g-h) at a spatial resolution of 40 m. Scatter plot between SDGSAT-1 at 40 m and ISS-P (e) in red (i), green (j), blue (k) and grayscale brightness (m). The symbol ** denotes that the correlation is significant at the 0.01 level (two-tailed). (For interpretation of the references to color in this figure legend, the reader is referred to the web version of this article.)

Fig. 5i), respectively. Combining the three bands' characteristics, the grayscale brightness correlation reached 0.57 between SDGSAT-1 and ISS-P (Fig. 5m). Overall, the quality of SDGSAT-1 NTL imagery was comparable to that of ISS-P.

4.2. *Characteristics of spatial variability in NTL*

We examined the differences in the NTL patterns of 4199 parcels in Beijing across 11 land-use types. The top two brightest areas were discovered to be commercial service and business offices, with mean values of 905 (DN) and 761 (DN), respectively (Fig. 6a). Interestingly, the sports and cultural areas had a mean value of 609 (DN), which was due to lighting from the essential sports facilities (Nest-type Beijing Olympic Stadium and Water Cube) and cultural facilities (National Theatre). The darkest areas belonged to the industrial area, with a mean value of 211 (DN). Most land use types in the red, green, blue, and brightness bands showed distinct differences. However, the land use regions with low NTL intensity were similar in the blue band, especially in industrial areas and greenspaces. Meanwhile, most land uses had the highest red brightness, followed by green brightness and then blue brightness. Importantly, by comparing Fig. 6a-b, the land use differentiation ability of the red, green, and blue bands of ISS-P was significantly weaker than that of SDGSAT-1, especially in the commercial area and business offices. This indicates that the satellite NTL data with higher radiometric resolution (16 bits) can better distinguish land use types in high-intensity areas than the spaceborne NTL data (8–14 bits) at the same resolution.

Spectral indexes can be used to enhance spectral features and further improve the differentiation of features (Verstraete and Pinty, 1996). The NDIGR significantly enhanced the contrast between greenspace and industrial areas (Fig. 7a), distinguishing them better using a single band image (Fig. 6a). The NDIBG further improved the differentiation of greenspace, educational, and commercial areas (Fig. 7b). Moreover, these two NTL indexes complemented each other. For example, the NDIBG cannot distinguish between residential and educational areas (Fig. 7b, Fig. 8b-I), which can be distinguished in the NDIGR (Fig. 7a, Fig. 8a-I). Thus, SONDI combines the advantages of these two indexes and can further improve its distinguishability in residential and educational areas (Fig. 7c and Fig. 8c-I). Similarly, the NDIGR cannot distinguish between business offices and administrative areas (Fig. 7a and Fig. 8a-II), which can be achieved in the SONDI (Fig. 7c and Fig. 8c-II). Therefore, selecting the appropriate SDGSAT-1 NTL index can provide support for land use classification.

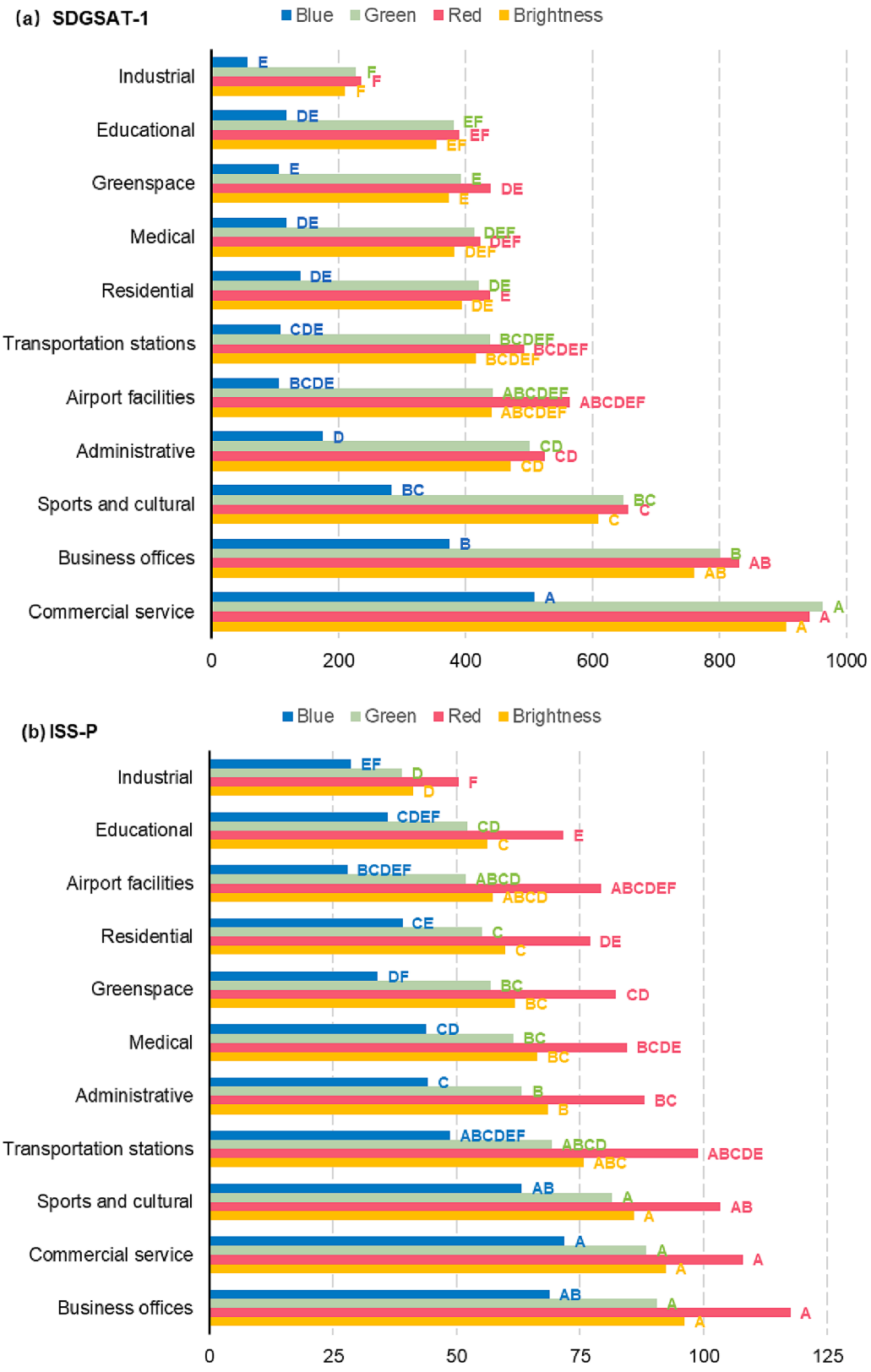

Fig. 6. ANOVA of the mean brightness for 11 land use types within the 5th Ring Road area of Beijing from the SDGSAT-1 (a) and ISS-P (b) NTL images. The label of each histogram denotes the ANOVA letters for each band and grayscale brightness. Land use categories not sharing the same letter were significantly different in their NTL brightness.

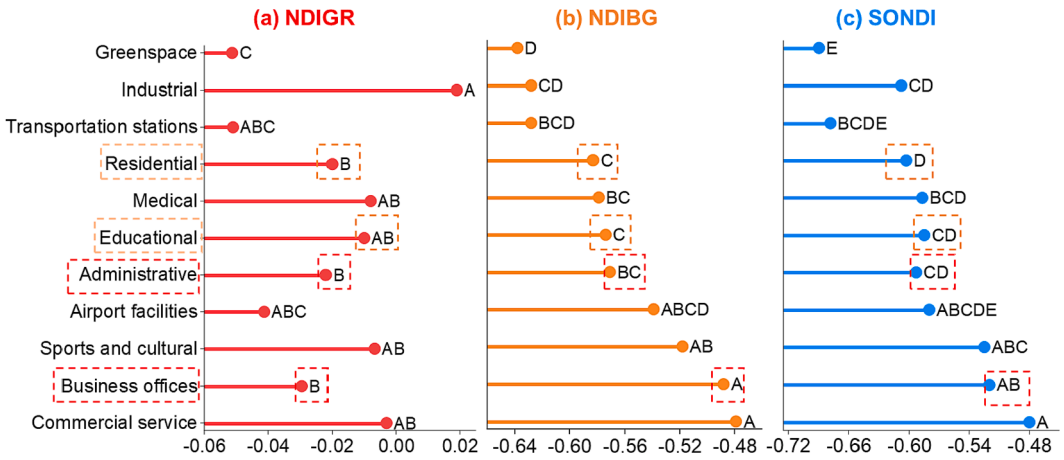

Fig. 7. ANOVA test of differences in mean index values of three NTL spectral indexes, i.e., NDIGR (a), NDIBG (b), and SONDI (c), for different land use types.

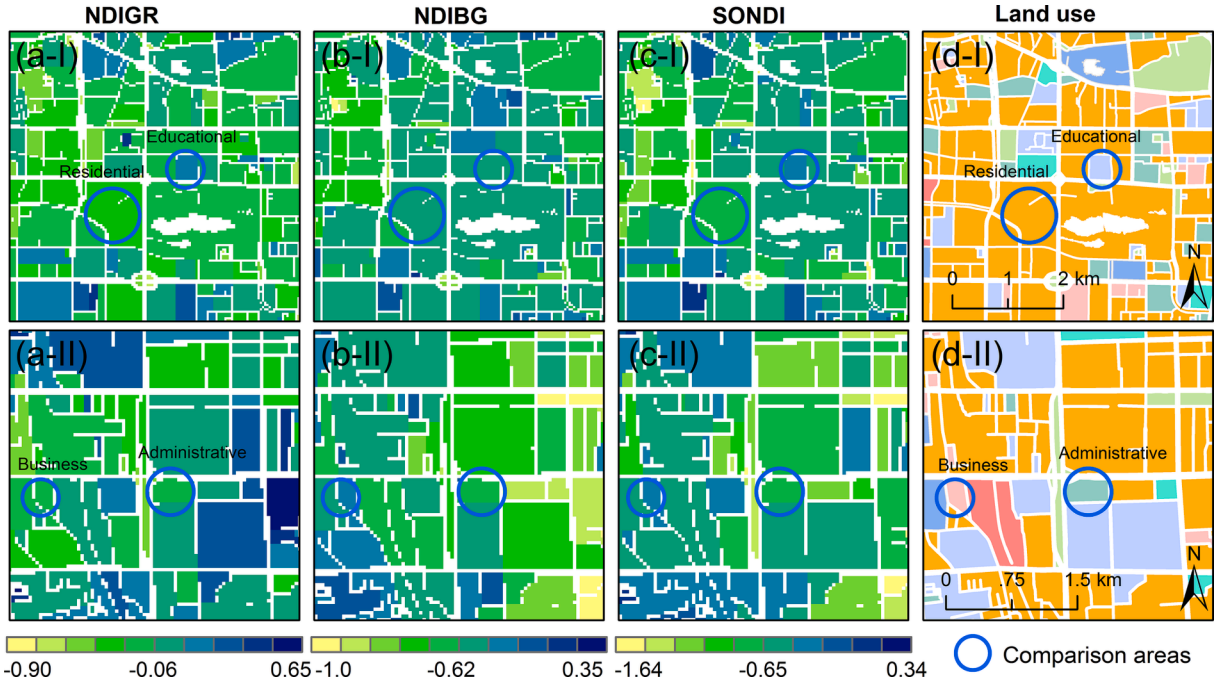

Fig. 8. The spatial pattern of three NTL spectral indexes at the parcel level. (a) NDIGR, (b) NDIBG, and (c) SONDI. The legend of land use (d) is the same as that of Fig. 2.

Table 4
The performance of four RF models in explaining SDGSAT-1 NTL spatial variability.

Metrics	Red	Green	Blue	Brightness
R^2	0.410	0.413	0.392	0.423
RMSE (DN)	0.265	0.253	0.408	0.254

4.3. The explanatory factors of the spatial variability in NTL

Table 4 and Fig. 9 present the results of the RF regression models for the RGB bands and grayscale brightness of parcel-level land-use areas as the response variables. A total of nine independent variables, including NDVI, RPOID, CPOID, IPOID, PPOID, GPOID, BD, BH, and RD, were found to explain 42.30% (R^2 = 0.423) of the brightness variability (Table 4). In the relative contribution of these independent variables to grayscale brightness, RD and IPOID were the most important and weakest factors, accounting for 24.23% and 7.33%, respectively. The remaining seven factors' contributions were almost 10% (Fig. 9). In the RGB models (Table 4), the blue band showed the lowest R^2 with a value of 0.392 and the highest RMSE with a value of 0.408 (DN). Meanwhile, the most important factor, i.e., PPOID (15.26%), in the blue band (Fig. 9) differed from the other two bands, i.e., RD (24.11% in the red light and 22.26% in the green light, Fig. 9). Therefore, blue light had the closest relationship with public facilities, and the other two colors of light showed the tightest correlation with road infrastructure.

5. Discussion

5.1. The quality of SDGSAT-1 NTL imagery

NTL brightness is dynamic owing to two groups of factors. The first category included external environmental factors such as human activity, vegetation phenology, surface albedo, atmospheric conditions, cloudiness, and the phase of the moon (Chen et al., 2019; Levin, 2017;

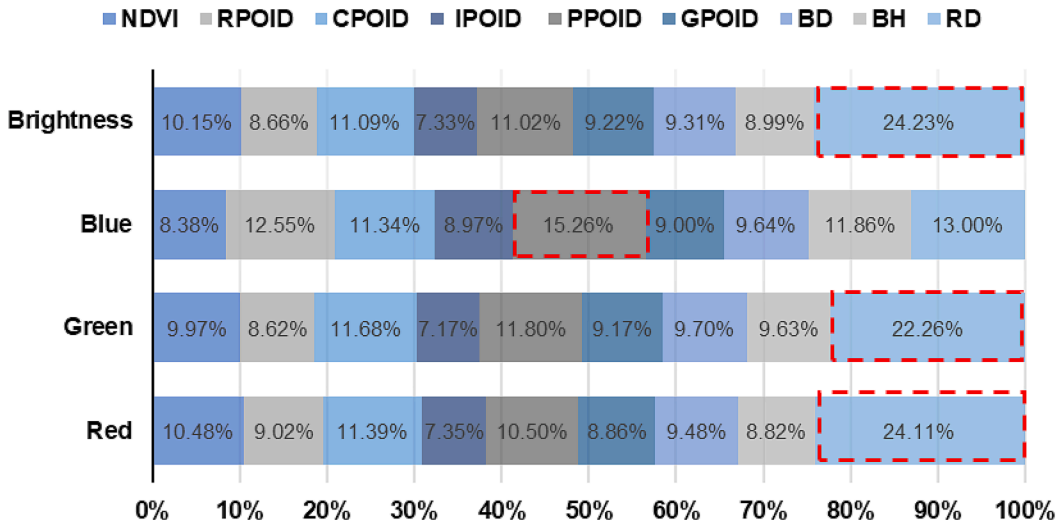

Fig. 9. The importance of explaining factors to SDGSAT-1 NTL mean value in red, green, blue bands, and gray brightness at the land use parcel level. The position of the red dotted box indicates the most important factor. (For interpretation of the references to color in this figure legend, the reader is referred to the web version of this article.)

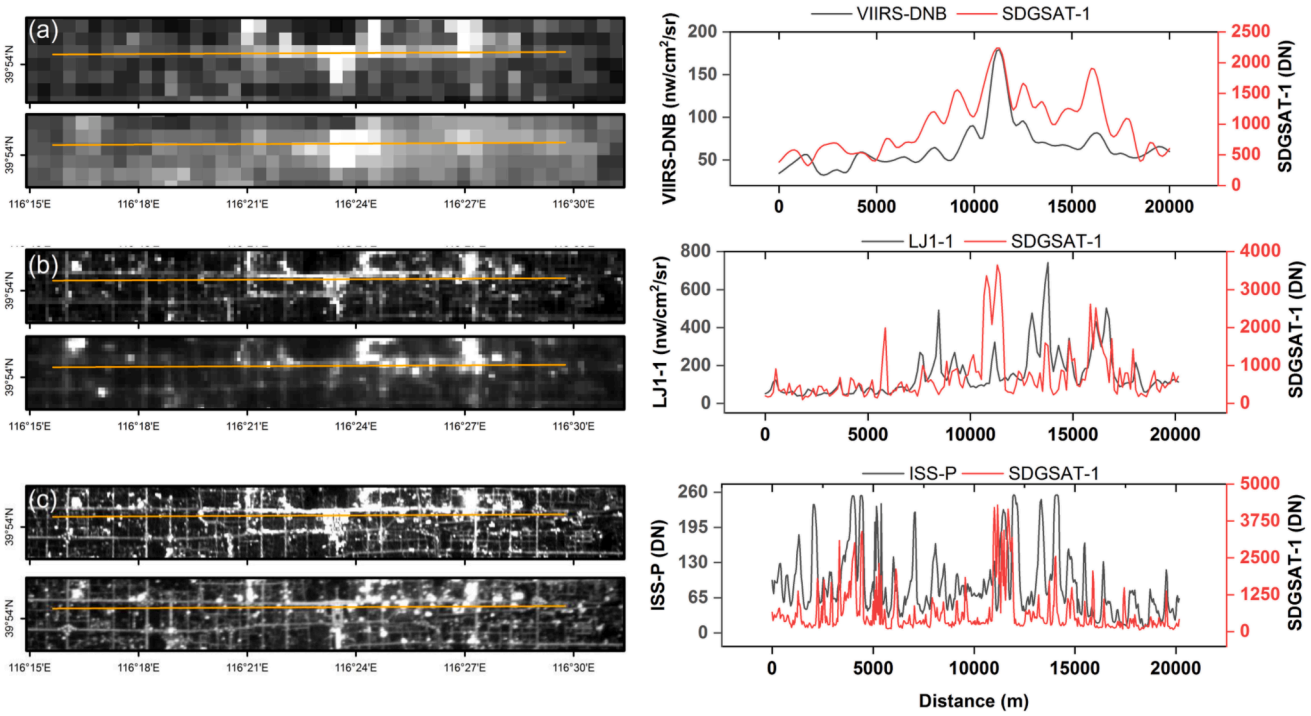

Fig. 10. Transect fluctuations of the pixel values between SDGSAT-1 (first row) and the other three NTL data (second row), including VIIRS-DNB (a, 500 m), LJ1-01 (b, 130 m), and ISS-P (c, 40 m) in Beijing.

Román et al., 2018). The second group was sensor imaging factors, such as spatial, radiometric, and spectral resolution, view angles, orbit height, and overpass time, which showed critical impacts on the pixel values of NTL (Guk and Levin, 2020; Li et al., 2020; Tan et al., 2022).

In this study, we tested the quality of the SDGSAT-1 NTL image via comparison analysis between it and existing NTL data, i.e., VIIRS-DNB, LJ1-01, and ISS-P data. Overall, the spatial pattern and pixel correlation of SDGSAT-1 maintained good consistency with the existing NTL data. In Fig. 4, the correlation between VIIRS-DNB and SDGSAT-1 ($r = 0.57$) was higher than that between LJ1-01 and SDGSAT-1 ($r = 0.51$). This result was similar to the findings of Guk and Levin (2020). There were two possible explanations for this result. The main reason is that the pixel-level NTL spatial variation becomes apparent with increasing spatial resolution (Wiens, 1989). The following reason is the intra-variation of the NTL. The VIIRS-DNB and SDGSAT-1 were in the same season (winter), but the LJ1-01 was not (autumn, Table 2). The comparison analysis between ISS-P and SDGSAT-1 fully demonstrated the quality of SDGSAT-1 (Fig. 5). Remarkably, the correlation between them was lowest in the blue band ($r = 0.46$) compared to the red ($r = 0.60$) and green ($r = 0.55$) bands. The reason for this is most likely due to atmospheric Rayleigh scattering, a detailed principle illustrating that light with shorter wavelengths is scattered more (Kocifaj et al., 2019). Thus, it is a daunting task to capture blue light accurately. Moreover, transect analysis was added to further confirm the ability of the SDGSAT-1 NTL

Table 5
The ratio of primary, secondary, and tertiary sectors to GDP in Beijing from 2014 to 2020.

Year	Primary sector (%)	Secondary sector (%)	Tertiary sector (%)
2014	0.69	19.34	79.97
2015	0.57	17.84	81.60
2016	0.48	17.25	82.27
2017	0.41	16.90	82.69
2018	0.36	16.55	83.09
2019	0.32	15.99	83.69
2020	0.30	15.83	83.87

image to capture detailed intraurban information (Fig. 10). The pixel values of the two NTL datasets both increased toward the core urban area and decreased toward the periphery (Fig. 10a-c). The variability of SDGSAT-1 was higher than that of VIIRS-DNB and LJ1-01 and similar to that of the ISS-P image. Therefore, the above results suggest that the quality of the SDGSAT-1 image is better than most existing NTLs in reflecting intraurban variability.

5.2. Spatial variability in NTL and explaining factors behind it

Following an examination of the quality of SDGSAT-1 data, the spatial variability in the NTL of land uses was investigated to fully utilize its high spatial resolution and RGB bands. Our results showed that

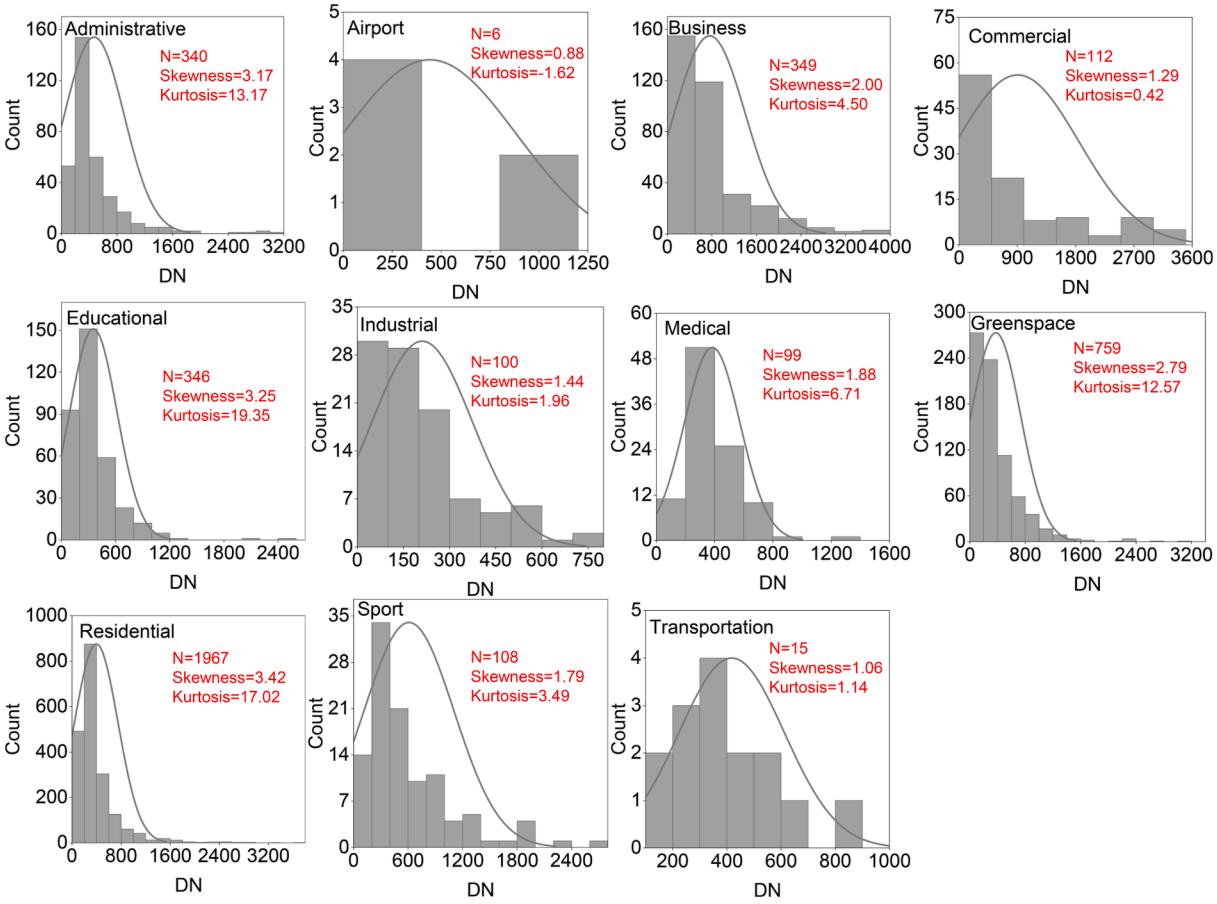

Fig. 11. Distribution of SDGSAT-1 brightness DN values of 11 parcel-level land use types.

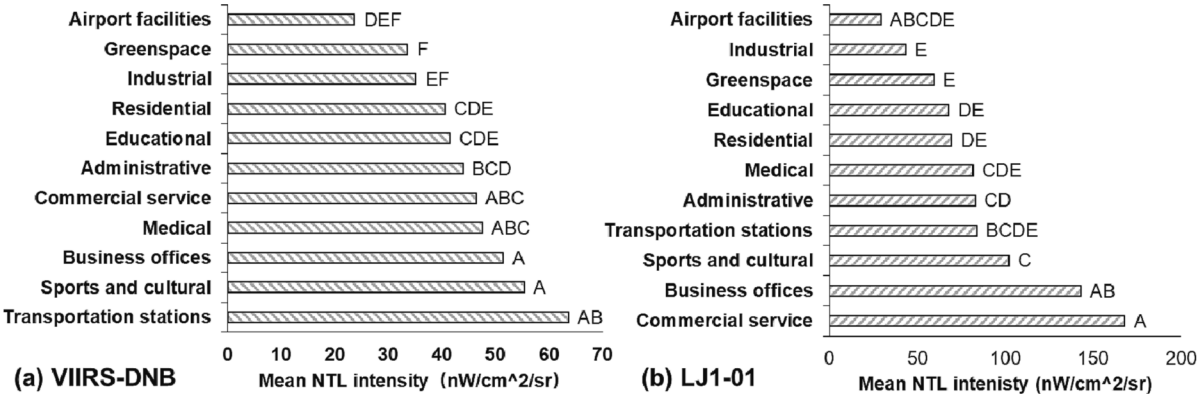

Fig. 12. ANOVA of differences in the mean brightness of VIIRS-DNB (a) and LJ1-01 (b) NTL for different land use classes.

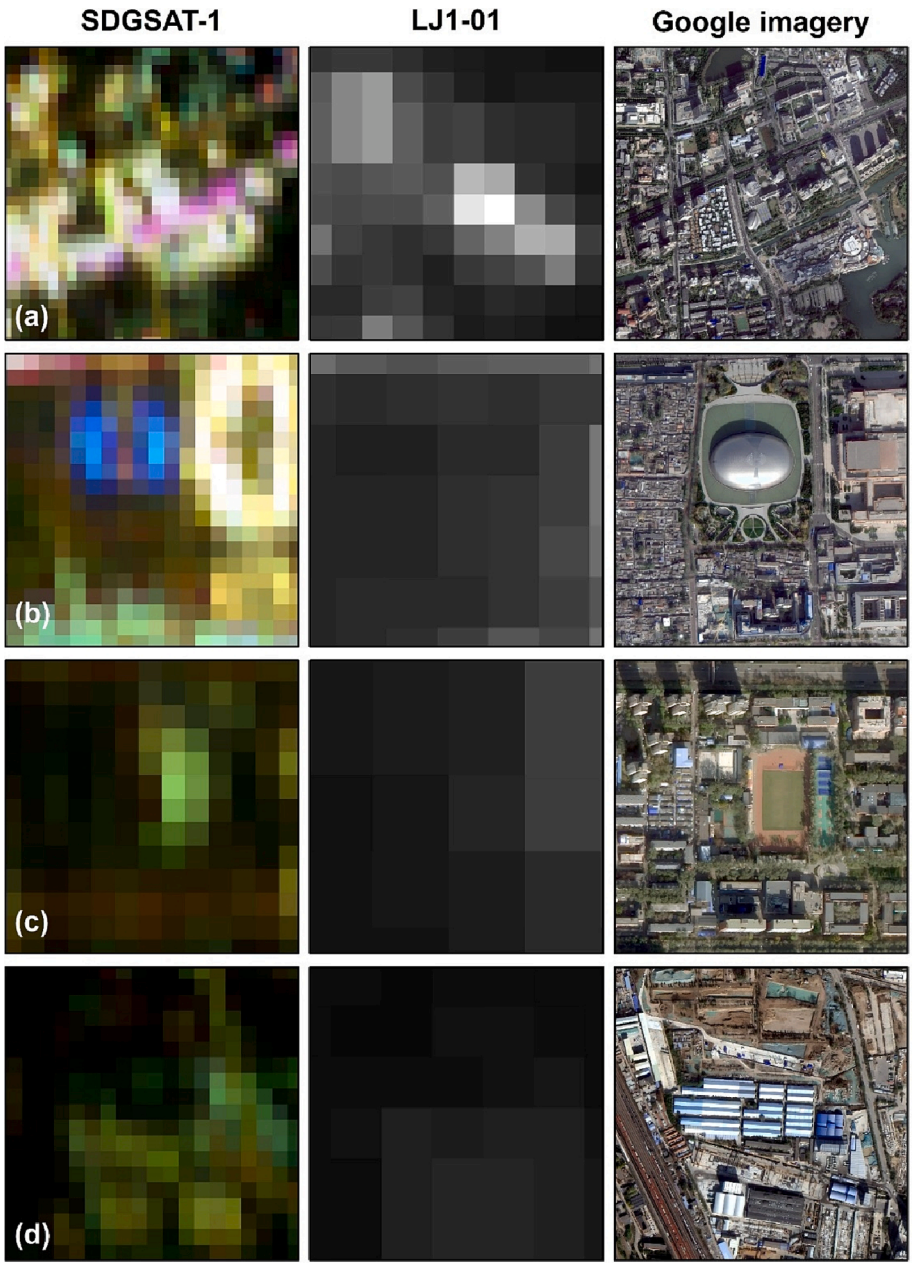

Fig. 13. SDGSAT-1 (left panel), LJ1-01 (middle panel) and Google images (right panel) of four selected regions, including residential area (a), cultural facilities (b), educational area (c), and industrial area (d).

SDGSAT-1 NTL grayscale brightness exhibited apparent differentiation in all land uses (Fig. 6a), which outperformed ISS-P (Fig. 6b). This result was in good accordance with the results of Guk and Levin. (2020). Some inconsistencies existed in the relative ranks between red-green bands and the lowest brightness of the industrial area. The possible reasons for this phenomenon were as follows: (1) these two study areas had different lighting patterns owing to the socioeconomic level, building features, and type of lighting facilities (Zheng et al., 2018); (2) most low-end industrial factories in Beijing have been removed to the adjacent city to relieve the noncapital function. This could be demonstrated in the ratio of the secondary sector to gross domestic product (GDP), which decreased by 3.51% from 2014 to 2020 (Table 5); and (3) The local overpass times of the SDGSAT-1 and JL-3B imagery were 9:00 pm and 10:00 pm.

The NTL value distribution of 11 land use types of SDGSAT-1 brightness reflected obvious variations in skewness ranging from 0.88 to 3.42 and kurtosis from −1. 62 to 19.35 (Fig. 11). This could further illustrate the intraurban variability of SDGSAT-1 NTL intensity across various land use parcels. Notably, the blue band of SDGSAT-1 represented poor distinguishability in low-light areas, i.e., industrial areas and greenspaces. This problem was also seen in the LJ1-01 NTL (Fig. 12b). By comparison, the VIIRS-DNB NTL could represent variability in these two land uses (Fig. 12a). The VIIRS-DNB performs better in dimly lit areas because its low light detection limit is 2E-10 W/cm^2/sr (Elvidge et al., 2013). Moreover, the NTL spectral index of SDGSAT-1 could further improve the capability of classifying land use types (Figs. 7-8). Therefore, the ability of SDGSAT-1 NTL imagery to reflect spatial variability in various land use parcels outperformed most of the previous NTL data.

The explanatory factors behind the spatial variability in the SDGSAT-1 NTL brightness were analyzed via RF regression models. The R^2 of the four models ranged from 39.20% to 42.30%, showing different levels of explaining NTL variability with existing studies (41%–50%) using JL1-3B data in Jerusalem (Guk and Levin, 2020). The differences between

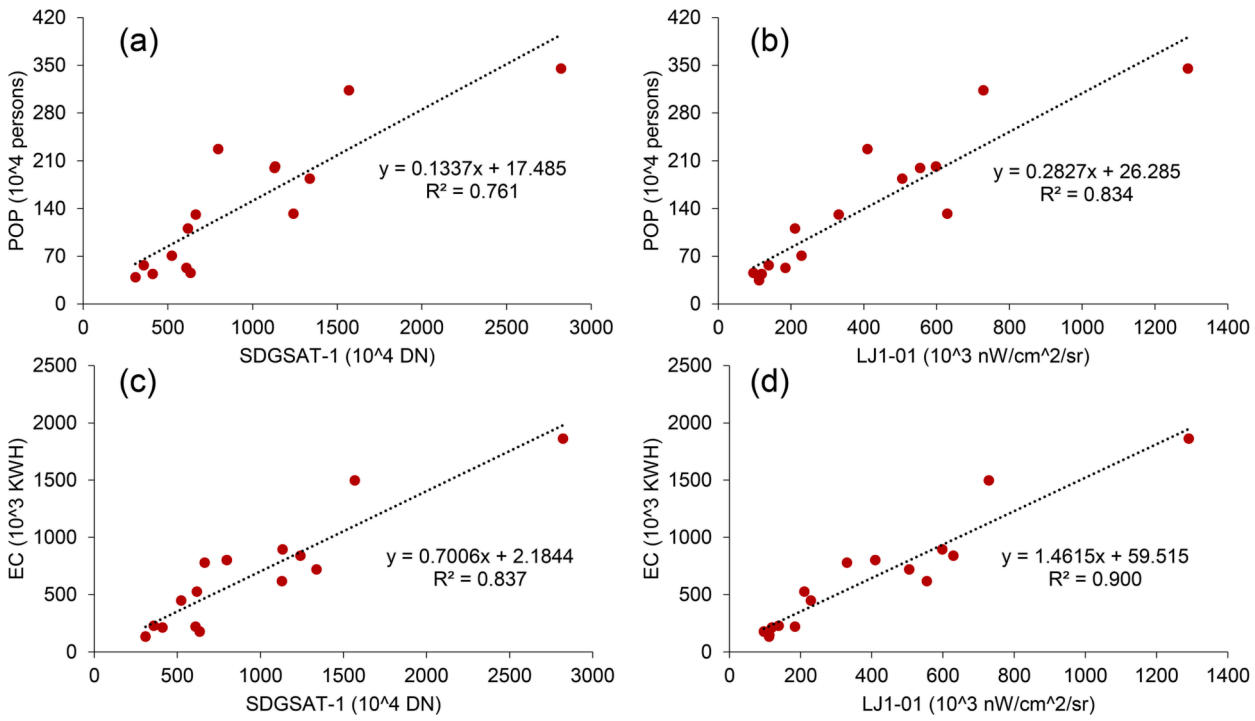

Fig. 14. Scatter plot between the sum of total light (SOTL) and socioeconomic parameters, i.e., population (POP) and electricity consumption (EC), at the district level in Beijing.

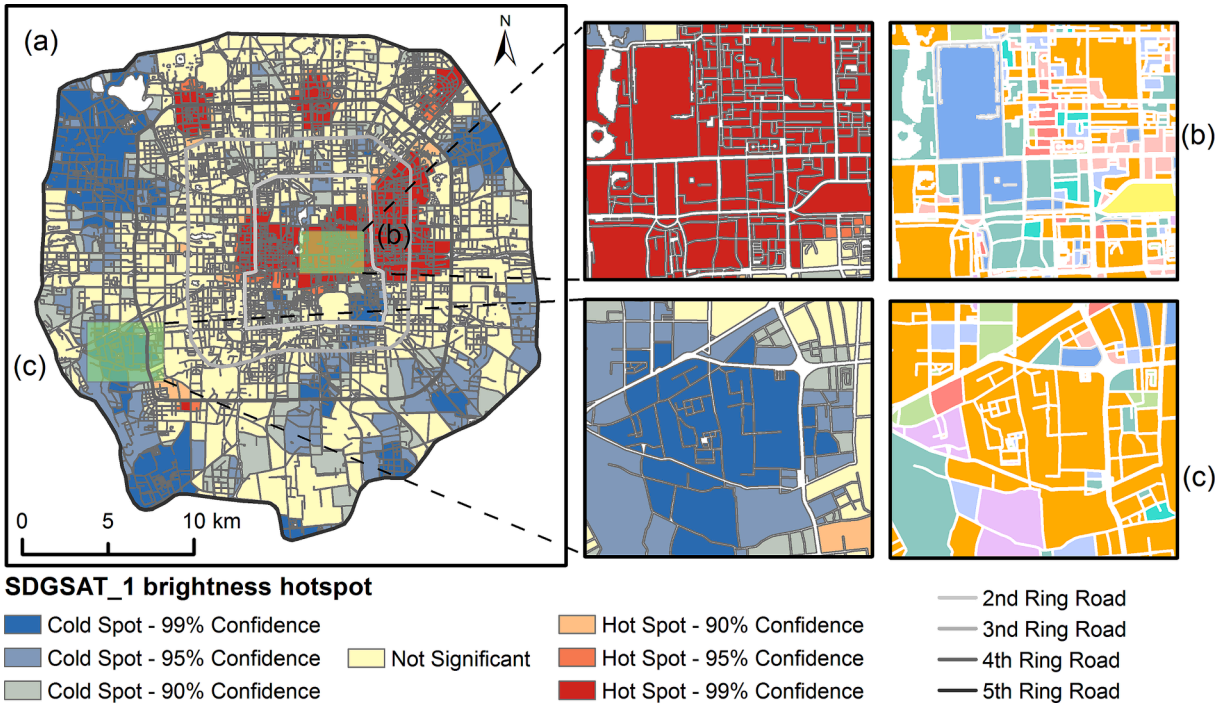

Fig. 15. SDGSAT-1 light brightness hotspots and coldspots. The legend of land use types is the same as in Fig. 2.

these two can be attributed to several reasons: the difference in the NTL features (spatial resolutions and overpass times of LJ1-3B and SDGSAT-1 (Elvidge et al., 2013)) and explanatory factors may result in different interpretation capabilities. Meanwhile, the highest importance score of the red and green bands as RD was different in the blue band, i.e., PPOID. From this result, HPS and LED lamps may be important lighting sources on roads (Fig. 1a) and in public areas, respectively.

5.3. Potential applications based on SDGSAT-1 NTL imagery

Based on the spatial variability of SDGSAT-1 NTL image in intensity and spectra, it could be applied to classify land use types combined with auxiliary data, extract the location of the lighting sources and distinguish their categories, i.e., HPS and LED (Fig. 13). It also suggests that NTL images derived from SDGSAT-1 could be used for other applications, such as mapping offshore fishing (Huang et al., 2022) and gas

Table 6
The area ratio of 11 land use types in the NTL hotspot and coldspot areas.

Land use	Ratio of hotspot areas (%)	Ratio of coldspot areas (%)
Residential	40.05	47.17
Business offices	18.27	2.61
Commercial service	4.05	2.61
Industrial	0.63	6.20
Transportation stations	0.36	0.27
Airport facilities	0.09	0.09
Administrative	12.06	5.57
Educational	6.39	6.92
Medical	2.70	1.53
Sports and cultural	4.14	1.26
Greenspace	11.25	25.79

flares (Levin et al., 2020). Moreover, the ability of SDGSAT-1 NTL imagery to estimate socioeconomic parameters was evaluated by linear regression in Fig. 14. The relationship between the sum of total light (SOTL) and two socioeconomic parameters (population (POP) and electricity consumption (EC)) was significantly positive, with R^2 values of 0.761 (Fig. 14a) and 0.837 (Fig. 14c). The accuracy between LJ1-01 NTL and the two parameters was higher than that of SDGSAT-1 (Fig. 14a-d), which may be explained by spatial scale effects in estimating socioeconomic parameters by remote sensing data (Wu and Li, 2009). It has been well documented that high-quality NTL data can better reveal the heterogeneity of urban economic activities (Gibson et al., 2021). Therefore, using SDGSAT-1 NTL images to estimate socioeconomic parameters could better reveal the inequity of socioeconomic development.

Notably, the SDGSAT-1 NTL image can be used to analyze the environmental impacts of blue lighting (Gaston and de Miguel, 2022) and further investigate urban lighting pollution (Jiang et al., 2018) at finer scales. The hotspot analysis was adopted to identify the priority areas for controlling lighting pollution at the parcel level. Fig. 15 shows that (1) hotspots were primarily distributed in the interior of the Fourth Ring Road (Fig. 15b), and (2) residential areas, business offices, administrative areas, and greenspace were the most common land use types in hotspot areas (Table 6). Therefore, some methods for mitigating light pollution need to be implemented in these priority areas, such as replacing lighting types, increasing lighting shielding, limiting the number of lights, and reducing the lighting duration (Gaston and de Miguel, 2022).

6. Limitations

It is also necessary to discuss the limitations of this study. First, the data quality of SDGSAT-1 sometimes needs to be further improved due to stripe effects. Although the image derived from SDGSAT-1 in this study was of high quality, the stripe problem of L1A NTL images greatly affects its applications (Zhang et al., 2022). This problem could be mitigated by the anomaly detection and spectral similarity restoration algorithm proposed by Zhang et al. (2022). Second, the quality examination of SDGSAT-1 NTL data lacks temporal imagery and field observations. Temporal NTL quality analysis is limited by data availability. The field observation of urban lighting will be conducted in the following work. Third, the study area is limited to Beijing. Therefore, the application area could be considered other typical cities in developed and developing regions.

6. Conclusions.

In this study, the capability of SDGSAT-1, new-generation NTL data with 40 m spatial resolution in multispectral bands, was examined, taking the capital of China, Beijing, as the study area. First, the quality of SDGSAT-1 NTL imagery was checked by comparison with two single-band NTLs, i.e., VIIRS-DNB and LJ1-01, and one multispectral NTL, ISS-P data. Second, intraurban spatial variability in NTL intensity and spectra at parcel-level land uses was analyzed by the ANOVA method. Third, the explanatory factors of NTL variability across different land uses were explored via RF regression. The results showed the following:

(1) The quality of the SDGSAT-1 NTL imagery remained consistent with that of previous NTL imagery. The correlation between VIIRS-DNB and SDGSAT-1 with an r-value of 0.57 was larger than LJ1-01 ($r = 0.51$). Moreover, there was a poor correlation in the blue band ($r = 0.46$) between ISS-P and SDGSAT-1, probably owing to atmospheric scattering.

(2) The effectiveness of SDGSAT-1 NTL imagery in distinguishing various land uses was demonstrated. Most land uses had different ranks of NTL intensity in three bands and grayscale brightness, which is better than the previous NTLs. Meanwhile, the NTL spectral index could further enhance the contrast of different land uses.

(3) The nine factors could explain the NTL intensity variability in three visible bands ranging from 39.20% to 41.30%. The most important factors in the red-green and blue bands were RD and PPOID. This is probably related to the distribution of HPS and LED lamps.

The above results illustrate the superiority of the SDGSAT-1 NTL product and the potentiality of SDGSAT-1 in reflecting intraurban spatial variability at parcel-level land use. It is anticipated that SDGSAT-1 NTL will enable advances in urban applications that have shown promise using previous NTL products, such as mapping urban areas and estimating socioeconomic parameters. Moreover, it could be beneficial to promote sustainable urban development by mapping land use for urban planning and analyzing urban artificial lighting pollution and the environmental impacts of blue lighting at a finer scale.

CRediT authorship contribution statement

Biyun Guo: Conceptualization, Methodology, Data curation, Visualization, Writing – original draft, Writing – review & editing. **Deyong Hu:** Conceptualization, Methodology, Supervision, Project administration, Funding acquisition, Writing – review & editing. **Qiming Zheng:** Conceptualization, Funding acquisition, Writing – review & editing.

Declaration of Competing Interest

The authors declare that they have no known competing financial interests or personal relationships that could have appeared to influence the work reported in this paper.

Data availability

The authors do not have permission to share data.

Acknowledgments

We gratefully thank the International Research Center of Big Data for Sustainable Development Goals, Amap, and Open Street Map for providing SDGSAT-1 nighttime light, POI, building, and road network vector data, respectively. This study was supported by the National Natural Science Foundation of China (No. 41671339) and the Start-up Fund for Research Assistant Professors recruited under the Strategic Hiring Scheme of the Hong Kong Polytechnic University (No. P0044791).

References

Belgiu, M., Drăgu, L., 2016. Random forest in remote sensing: A review of applications and future directions. ISPRS J. Photogramm. Remote Sens. 114, 24–31. https://doi.org/10.1016/J.ISPRSJPRS.2016.01.011.

Chang, D., Wang, Q., Yang, J., Xu, W., 2022. Research on Road Extraction Method Based on Sustainable Development Goals Satellite-1 Nighttime Light Data. Remote Sens. 14, 6015. https://doi.org/10.3390/RS14236015.

Chen, Z., Yu, B., Ta, N., Shi, K., Yang, C., Wang, C., Zhao, X., Deng, S., Wu, J., 2019. Delineating Seasonal Relationships between Suomi NPP-VIIRS Nighttime Light and Human Activity across Shanghai, China. IEEE J. Sel. Top. Appl. Earth Obs. Remote Sens. 12, 4275–4283. https://doi.org/10.1109/JSTARS.2019.2916323.

Chen, Z., Wei, Y., Shi, K., Zhao, Z., Wang, C., Wu, B., Qiu, B., Yu, B., 2022. The potential of nighttime light remote sensing data to evaluate the development of digital economy: A case study of China at the city level. Comput. Environ. Urban Syst. 92, 101749 https://doi.org/10.1016/J.COMPENVURBSYS.2021.101749.
Elvidge, C.D., Baugh, K.E., Kihn, E.A., Kroehl, H.W., Davis, E.R., 1997. Mapping City Lights With Nighttime Data from the DMSP Operational Linescan System. Photogramm. Eng. Remote Sensing 63, 727–734.
Elvidge, C.D., Cinzano, P., Pettit, D.R., Arvesen, J., Sutton, P., Small, C., Nemani, R., Longcore, T., Rich, C., Safran, J., Weeks, J., Ebener, S., 2007. The Nightsat mission concept. Int. J. Remote Sens. 28, 2645–2670. https://doi.org/10.1080/01431160600981525.
Elvidge, C.D., Baugh, K.E., Zhizhin, M., Hsu, F.-C., 2013. Why VIIRS data are superior to DMSP for mapping nighttime lights. Proc. Asia-Pacific Adv. Netw. 35, 62. https://doi.org/10.7125/APAN.35.7.
Elvidge, C.D., Zhizhin, M., Ghosh, T., Hsu, F.C., Taneja, J., 2021. Annual Time Series of Global VIIRS Nighttime Lights Derived from Monthly Averages: 2012 to 2019. Remote Sens. 13, 922. https://doi.org/10.3390/RS13050922.
Fu, Y., Li, J., Weng, Q., Zheng, Q., Li, L., Dai, S., Guo, B., 2019. Characterizing the spatial pattern of annual urban growth by using time series Landsat imagery. Sci. Total Environ. 666, 274–284. https://doi.org/10.1016/j.scitotenv.2019.02.178.
Gaston, K.J., de Miguel, A.S., 2022. Environmental Impacts of Artificial Light at Night. Annu. Rev. Environ. Resour. 47 https://doi.org/10.1146/ANNUREV-ENVIRON-112420-014438.
Gibson, J., Olivia, S., Boe-Gibson, G., Li, C., 2021. Which night lights data should we use in economics, and where? J. Dev. Econ. 149, 102602 https://doi.org/10.1016/J.JDEVECO.2020.102602.
Gong, P., Chen, B., Li, X., Liu, H., Wang, J., Bai, Y., Chen, J., Chen, X., Fang, L., Feng, S., Feng, Y., Gong, Y., Gu, H., Huang, H., Huang, X., Jiao, H., Kang, Y., Lei, G., Li, A., Li, X., Li, X., Li, Y., Li, Z., Li, Z., Liu, C., Liu, C., Liu, M., Liu, S., Mao, W., Miao, C., Ni, H., Pan, Q., Qi, S., Ren, Z., Shan, Z., Shen, S., Shi, M., Song, Y., Su, M., Ping Suen, H., Sun, B., Sun, F., Sun, J., Sun, L., Sun, W., Tian, T., Tong, X., Tseng, Y., Tu, Y., Wang, H., Wang, L., Wang, X., Wang, Z., Wu, T., Xie, Y., Yang, J., Yang, J., Yuan, M., Yue, W., Zeng, H., Zhang, K., Zhang, N., Zhang, T., Zhang, Y., Zhao, F., Zheng, Y., Zhou, Q., Clinton, N., Zhu, Z., Xu, B., 2020. Mapping essential urban land use categories in China (EULUC-China): preliminary results for 2018. Sci. Bull. 65, 182–187. https://doi.org/10.1016/J.SCIB.2019.12.007.
Grundland, M., Dodgson, N.A., 2007. Decolorize: Fast, contrast enhancing, color to grayscale conversion. Pattern Recognit. 40, 2891–2896. https://doi.org/10.1016/J.PATCOG.2006.11.003.
Guk, E., Levin, N., 2020. Analyzing spatial variability in night-time lights using a high spatial resolution color Jilin-1 image – Jerusalem as a case study. ISPRS J. Photogramm. Remote Sens. 163, 121–136. https://doi.org/10.1016/J.ISPRSJPRS.2020.02.016.
Guo, H., Dou, C., Chen, H., Liu, J., Fu, B., Li, X., Zou, Z., Liang, D., 2023. SDGSAT-1: the world's first scientific satellite for sustainable development goals. Sci. Bull. 68, 34–38. https://doi.org/10.1016/J.SCIB.2022.12.014.
Hu, S., Ge, Y., Liu, M., Ren, Z., Zhang, X., 2022. Village-level poverty identification using machine learning, high-resolution images, and geospatial data. Int. J. Appl. Earth Obs. Geoinf. 107, 102694 https://doi.org/10.1016/J.JAG.2022.102694.
Huang, R., Wu, W., Yu, K., 2022. Building consistent time series night-time light data from average DMSP/OLS images for indicating human activities in a large-scale oceanic area. Int. J. Appl. Earth Obs. Geoinf. 114, 103023 https://doi.org/10.1016/J.JAG.2022.103023.
Jiang, W., He, G., Long, T., Guo, H., Yin, R., Leng, W., Liu, H., Wang, G., 2018. Potentiality of Using Luojia 1–01 Nighttime Light Imagery to Investigate Artificial Light Pollution. Sensors 18, 2900. https://doi.org/10.3390/s18092900.
Jin, K., Wang, F., Chen, D., Liu, H., Ding, W., Shi, S., 2019. A new global gridded anthropogenic heat flux dataset with high spatial resolution and long-term time series. Sci. Data 1–14. https://doi.org/10.1038/s41597-019-0143-1.
Kocifaj, M., Solano-Lamphar, A., Videen, G., 2019. Night-sky radiometry can revolutionize the characterization of light-pollution sources globally. Proc. Natl. Acad. Sci. U. S. A. 116, 7712–7717. https://doi.org/10.2307/26703328.
Levin, N., 2017. The impact of seasonal changes on observed nighttime brightness from 2014 to 2015 monthly VIIRS DNB composites. Remote Sens. Environ. 193, 150–164. https://doi.org/10.1016/J.RSE.2017.03.003.
Levin, N., Kyba, C.C.M., Zhang, Q., Sánchez de Miguel, A., Román, M.O., Li, X., Portnov, B.A., Molthan, A.L., Jechow, A., Miller, S.D., Wang, Z., Shrestha, R.M., Elvidge, C.D., 2020. Remote sensing of night lights: A review and an outlook for the future. Remote Sens. Environ. 237, 111443 https://doi.org/10.1016/J.RSE.2019.111443.
Li, K., Chen, Y., Li, Y., 2018a. The Random Forest-Based Method of Fine-Resolution Population Spatialization by Using the International Space Station Nighttime Photography and Social Sensing Data. Remote Sens. 10, 1650. https://doi.org/10.3390/RS10101650.
Li, X., Li, D., Xu, H., Wu, C., 2017. Intercalibration between DMSP/OLS and VIIRS night-time light images to evaluate city light dynamics of Syria's major human settlement during Syrian Civil War. Int. J. Remote Sens. 38, 5934–5951. https://doi.org/10.1080/01431161.2017.1331476.
Li, X., Zhao, L., Li, D., Xu, H., 2018b. Mapping Urban Extent Using Luojia 1–01 Nighttime Light Imagery. Sensors 18, 3665. https://doi.org/10.3390/s18113665.
Li, X., Levin, N., Xie, J., Li, D., 2020. Monitoring hourly night-time light by an unmanned aerial vehicle and its implications to satellite remote sensing. Remote Sens. Environ. 247, 111942 https://doi.org/10.1016/J.RSE.2020.111942.
Li, X.i., Li, X., Li, D., He, X., Jendryke, M., 2019. A preliminary investigation of Luojia-1 night-time light imagery. Remote Sens. Lett. 10, 526–535. https://doi.org/10.1080/2150704X.2019.1577573.
Lin, Z., Jiao, W., Liu, H., Long, T., Liu, Y., Wei, S., He, G., Portnov, B.A., Trop, T., Liu, M., Li, X., Wen, C., 2023. Modelling the Public Perception of Urban Public Space Lighting Based on SDGSAT-1 Glimmer Imagery: A Case Study in Beijing. China. Sustain. Cities Soc. 88, 104272 https://doi.org/10.1016/J.SCS.2022.104272.
Liu, X., Huang, Y., Xu, X., Li, X., Li, X., Ciais, P., Lin, P., Gong, K., Ziegler, A.D., Chen, A., Gong, P., Chen, J., Hu, G., Chen, Y., Wang, S., Wu, Q., Huang, K., Estes, L., Zeng, Z., 2020. High-spatiotemporal-resolution mapping of global urban change from 1985 to 2015. Nat. Sustain. 3, 564–570. https://doi.org/10.1038/s41893-020-0521-x.
Ma, T., 2018. An Estimate of the Pixel-Level Connection between Visible Infrared Imaging Radiometer Suite Day/Night Band (VIIRS DNB) Nighttime Lights and Land Features across China. Remote Sens. 10, 723. https://doi.org/10.3390/RS10050723.
Román, M.O., Wang, Z., Sun, Q., Kalb, V., Miller, S.D., Molthan, A., Schultz, L., Bell, J., Stokes, E.C., Pandey, B., Seto, K.C., Hall, D., Oda, T., Wolfe, R.E., Lin, G., Golpayegani, N., Devadiga, S., Davidson, C., Sarkar, S., Praderas, C., Schmaltz, J., Boller, R., Stevens, J., Ramos González, O.M., Padilla, E., Alonso, J., Detrés, Y., Armstrong, R., Miranda, I., Conte, Y., Marrero, N., MacManus, K., Esch, T., Masuoka, E.J., 2018. NASA's Black Marble nighttime lights product suite. Remote Sens. Environ. 210, 113–143. https://doi.org/10.1016/J.RSE.2018.03.017.
Sánchez de Miguel, A., Kyba, C.C.M., Aubé, M., Zamorano, J., Cardiel, N., Tapia, C., Bennie, J., Gaston, K.J., 2019. Colour remote sensing of the impact of artificial light at night (I): The potential of the International Space Station and other DSLR-based platforms. Remote Sens. Environ. 224, 92–103. https://doi.org/10.1016/J.RSE.2019.01.035.
Sánchez de Miguel, A., Bennie, J., Rosenfeld, E., Dzurjak, S., Gaston, K.J., 2022. Environmental risks from artificial nighttime lighting widespread and increasing across Europe. Sci. Adv. 8, eabl6891. https://doi.org/10.1126/SCIADV.ABL6891/SUPPL_FILE/SCIADV.ABL6891_DATA_S1_AND_S2.ZIP.
Tan, X., Zhu, X., Chen, J., Chen, R., 2022. Modeling the direction and magnitude of angular effects in nighttime light remote sensing. Remote Sens. Environ. 269, 112834 https://doi.org/10.1016/J.RSE.2021.112834.
Verstraete, M.M., Pinty, B., 1996. Designing optimal spectral indexes for remote sensing applications. IEEE Trans. Geosci. Remote Sens. 34, 1254–1265. https://doi.org/10.1109/36.536541.
Wang, N., Hu, Y., Li, X.M., Kang, C., Yan, L., 2023. AOD Derivation from SDGSAT-1/GLI Dataset in Mega-City Area. Remote Sens. 15, 1343. https://doi.org/10.3390/RS15051343.
Wang, M., Zhang, F., Wu, F., 2022. Governing urban redevelopment: A case study of Yongqingfang in Guangzhou. China. Cities 120, 103420. https://doi.org/10.1016/J.CITIES.2021.103420.
Wiens, J.A., 1989. Spatial Scaling in Ecology. Funct. Ecol. 3, 385–397.
Wu, H., Li, Z.L., 2009. Scale Issues in Remote Sensing: A Review on Analysis, Processing and Modeling. Sensors 9, 1768–1793. https://doi.org/10.3390/S90301768.
Yang, L., Driscol, J., Sarigai, S., Wu, Q., Chen, H., Lippitt, C.D., 2022. Google Earth Engine and Artificial Intelligence (AI): A Comprehensive Review. Remote Sens. 2022, Vol. 14, Page 3253 14, 3253. https://doi.org/10.3390/RS14143253.
Zhang, D., Cheng, B., Shi, L., Gao, J., Long, T., Chen, B., Wang, G., 2022. A Destriping Algorithm for SDGSAT-1 Nighttime Light Images Based on Anomaly Detection and Spectral Similarity Restoration. Remote Sens. 2022, Vol. 14, Page 5544 14, 5544. https://doi.org/10.3390/RS14215544.
Zhang, Q., Schaaf, C., Seto, K.C., 2013. The Vegetation Adjusted NTL Urban Index: A new approach to reduce saturation and increase variation in nighttime luminosity. Remote Sens. Environ. 129, 32–41. https://doi.org/10.1016/J.RSE.2012.10.022.
Zhao, S., Liu, Y., Zhang, R., Fu, B., 2020. China's population spatialization based on three machine learning models. J. Clean. Prod. 256, 120644 https://doi.org/10.1016/J.JCLEPRO.2020.120644.
Zheng, Q., Weng, Q., Huang, L., Wang, K., Deng, J., Jiang, R., Ye, Z., Gan, M., 2018. A new source of multi-spectral high spatial resolution night-time light imagery—JL1-3B. Remote Sens. Environ. 215, 300–312. https://doi.org/10.1016/J.RSE.2018.06.016.
Zheng, Q., Weng, Q., Wang, K., 2021. Characterizing urban land changes of 30 global megacities using nighttime light time series stacks. ISPRS J. Photogramm. Remote Sens. 173, 10–23. https://doi.org/10.1016/j.isprsjprs.2021.01.002.
Zhou, Y., Li, X., Asrar, G.R., Smith, S.J., Imhoff, M., 2018. A global record of annual urban dynamics (1992–2013) from nighttime lights. Remote Sens. Environ. 219, 206–220. https://doi.org/10.1016/J.RSE.2018.10.015.